Fracturing and Near-Surface Diagenesis of a Silicified Miocene Deltaic Sequence: The Montjuïc Hill (Barcelona)

Irene Cantarero [1],*, David Parcerisa [2], Maria Alexandra Plata [1], David Gómez-Gras [3], Enrique Gomez-Rivas [1], Juan Diego Martín-Martín [1] and Anna Travé [1]

[1] Departament de Mineralogia, Petrologia i Geologia Aplicada. Facultat de Ciències de la Terra, Universitat de Barcelona (UB), C/Martí i Franqués s/n, 08028 Barcelona, Spain; alexa854@gmail.com (M.A.P.); e.gomez-rivas@ub.edu (E.G.-R.); juandiegomartin@ub.edu (J.D.M.-M.); atrave@ub.edu (A.T.)

[2] Departament d'Enginyeria Minera, Industrial i TIC, Escola Politècnica Superior d'Enginyeria de Manresa, Universitat Politècnica de Catalunya, Av. Bases de Manresa 63-71, 08242 Manresa, Spain; dparcerisa@epsem.upc.edu

[3] Departament de Geologia, Universitat Autònoma de Barcelona, 08193 Bellaterra (Cerdanyola del Vallès), Spain; David.Gomez@uab.cat

* Correspondence: i_cantarero@ub.edu; Tel.: +34-934031165

Abstract: Near-surface diagenesis has been studied in the Langhian siliciclastic rocks of the Montjuïc Hill (Barcelona Plain) by means of petrographical (optical and cathodoluminescence) and geochemical (electron microprobe, $\delta^{18}O$, $\delta^{13}C$, $\delta^{34}S$ and $^{87}Sr/^{86}Sr$) analyses. In the hill, these rocks are affected by strong silicification, but the same unit remains non-silicified at depth. The results reveal that fracturing took place after lithification and during uplift. Fracture cementation is clearly controlled by the previous diagenesis of the host rock. In non-silicified areas, cementation is dominated by calcite, which precipitated from meteoric waters. In silicified areas, fractures show multiepisodic cementation produced firstly by barite and secondly by silica, following the sequence opal, lussatite, chalcedony, and quartz. Barite precipitated only in fractures from the mixing of upflowing seawater and percolating meteoric fluids. The presence of silica stalactites, illuviation, and geopetal structures, and $\delta^{18}O$ values indicate that silica precipitation occurred in the vadose regime from low-temperature percolating meteoric fluids, probably during a glacial period. Moreover, the presence of alunite suggests that silica cement formed under acidic conditions. Karst features (vugs and caverns), formed by arenisation, reveal that silica was derived from the dissolution of surrounding silicified host rocks.

Keywords: silicification; meteoric diagenesis; fractures; deltaic sequence; karst; glacial period

1. Introduction

Depending on the depositional environment, interstitial waters in deltaic depositional systems can be of meteoric or marine origin, or a mixture of both [1] but can be modified due to relative sea-level fluctuations [1–5]. However, other external factors not related to the depositional system, such as fracturing, can also control the type and distribution of fluids. Fractures can act as conduits for fluids, which can be external fluids with different chemical and/or thermal properties or as barriers, causing compartmentalization of the system. Thus, the quality and heterogeneity of deltaic reservoirs depend on the depositional facies, diagenesis, and the presence of fractures [6–11]. Accordingly, the systematic study of cements, in both host rocks and fractures, can provide valuable information about the origin of fluids, the degree of fluid-rock interaction, the paleofluid flow paths, and the role of fractures for fluid transport [12–18].

Common early diagenetic processes in sandstones are burrowing and boring, cementation, often as concretions (typically of carbonate minerals, iron oxides, and phosphates), and soil formation [5,19]. Quartz and silica minerals are some of the most abundant cements in sandstones. Despite that, silicification processes are usually related to burial diagenesis and hydrothermalism [18,20–22], silicification can also develop in the form of chert or silcrete in near-surface conditions at relatively low temperatures [23–26]. Recent studies have demonstrated that different silicification events, starting with low temperature and followed by high-temperature silicification, had strongly modified the petrophysical properties of pre-salt carbonate reservoirs of the Campos and Santos Basin (offshore Brazil) and in the Kwanza Basin (offshore Angola) [27,28].

In the Catalan Coastal Ranges (NE Spain), previous studies show that the main diagenetic processes linked to Cenozoic and Mesozoic deformation events are calcite cementation and dolomitization ([15,29–37]). Only two locations have been found to show extensive silicification, both related to the Neogene extension: the Camp dels Ninots (Caldes de Malavella) and the Montjuïc Hill (in the city of Barcelona). In the Camp dels Ninots, silicification is represented by opaline chert nodules developed in maar-diatreme lake sediments, that is, in Pliocene sediments deposited in a lake that formed in a volcanic crater caused by a phreatomagmatic eruption. This silicification was produced by hydrothermal fluids associated with Neogene NW–SE normal faults and Pliocene volcanism [38]. On the contrary, the Montjuïc hill is a horst delimited by Neogene NE–SW normal faults and the silicification of its deltaic sequence has been attributed to low-temperature meteoric fluids [39–42].

In this contribution, we focus on the complex fracture diagenesis developed in previously silicified sandstones of a Miocene deltaic sequence in the Montjuïc Hill. Specifically, the aims of this study are fivefold: (i) to petrologically and geochemically characterize the successive generations of fracture-filling cements; (ii) to determine the composition and origin of fluids that circulated along the faults; (iii) to unravel the paleofluid pathways; (iv) to infer possible paleoclimatic implications from silica cements in fractures; and, (v) to determine the source of silica in fractures.

2. Geological Setting

The Catalan Coastal Ranges (CCR) in the NE of Spain, constitutes the northwestern edge of the Valencia Trough, which opened during the Neogene extensional event (Oligocene–Middle Miocene, [43]) (Figure 1A). During this extension, the CCR acquired a well-developed horst and graben structure limited by listric faults striking NE–SW and NNE–SSW with a detachment level at 12–16 km [44,45] (Figure 1B). This structure was also segmented by later faults trending NW–SE to NNW–SSE. The Neogene extensional event has been divided into a syn-rift stage (Aquitanian–Late Burdigalian), an early post-rift stage (Langhian–Serravallian), and a late post-rift stage (late Serravallian–Pliocene) [46]. Two small compressional episodes are recognized during the Neogene extension: one between the late Langhian–Serravalian (early post-rift) and the other during the Messinian (late post-rift) [45].

One of the grabens that formed at this time is the Barcelona Plain, a ~40 km long and ~2–10 km wide graben situated in the central sector of the CCR, and mainly filled with Miocene continental-transitional siliciclastic deposits and Quaternary fluvio-deltaic deposits. Its northern boundary is limited by the Collserola-Montnegre Horst, which is mainly formed by Paleozoic rocks consisting of Cambro-Ordovician shales and phyllites, Silurian black shales and phyllites, Devonian carbonates, Carboniferous Culm facies, and late Hercynian leucogranites, tonalites, and granodiorites [47]. The Montjuïc Hill is a tilted horst formed within the Miocene sediments filling the Barcelona Plain. It is bounded to the SE by the Morrot fault, a NE–SW normal fault that dips to the SE with a minimum vertical throw of 215 m [41] (Figure 2). It has been postulated that this block is also bounded to the NW by another NE–SW normal fault that dips to the NW [48,49].
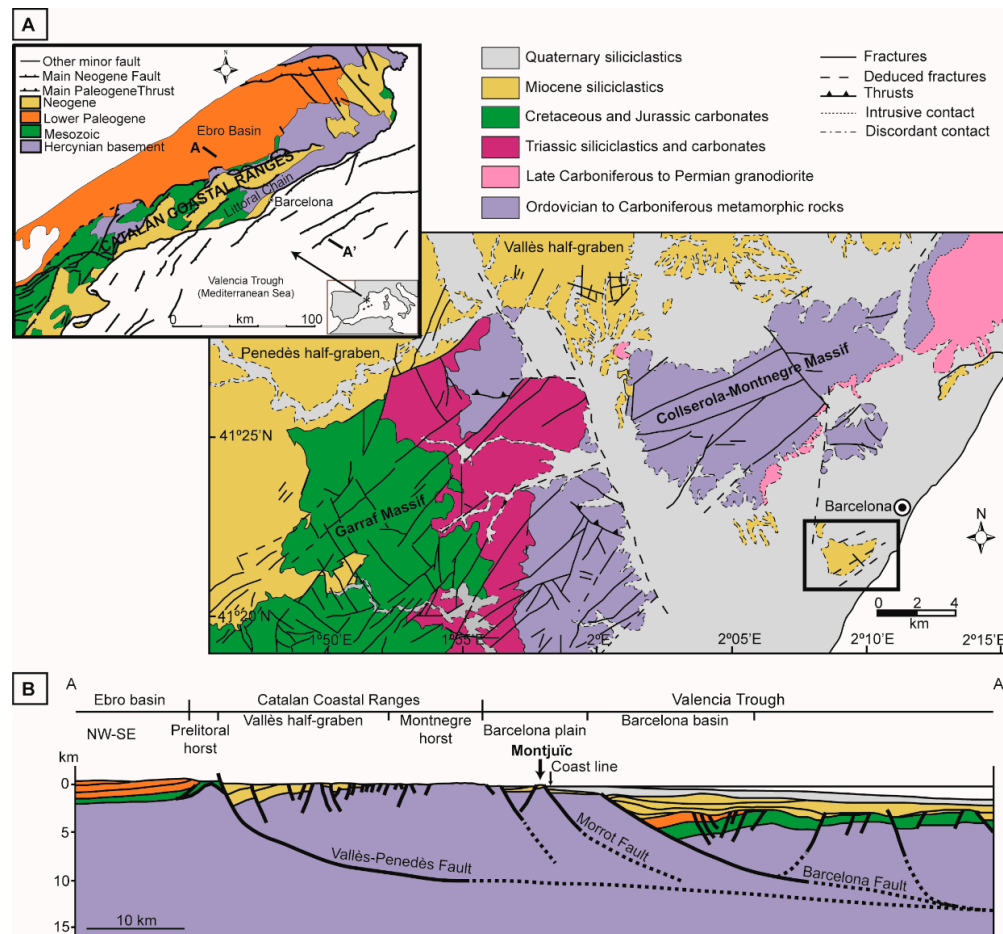
Figure 1. Geological setting. (**A**) Location and schematic map of the Catalan Coastal Ranges and magnification of the Littoral Chain around the study area. The Montjuïc Hill is marked with a black square. (**B**) Cross-section of the CCR indicated in (**A**) [45].

The Montjuïc block is formed by alternating sandstones and conglomerates units and minor lutitic beds interpreted as a prograding deltaic sequence of Serravallian age [40,41]. However, recent biostratigraphy studies place the planktonic zonations N9 and N10 of [50] in the Langhian [51]. Four lithostratigraphic units from base to top have been defined [40] (Figure 2): (1) The basal Morrot unit, formed by 80 m of conglomerates and sandstones, interpreted as delta plain deposits; (2) The Castell unit, represented by 100 m of siltstones and mudstones and well-cemented conglomerates and sandstones, interpreted as delta-front deposits; (3) The Miramar unit, defined by 15 m of marls, interpreted as prodelta deposits, and finally, (4) The Mirador unit, formed by 20 m of massive conglomerates and sandstones, interpreted as proximal delta-front deposits. The uplift of the hill took place between the Pliocene and the Quaternary, according to the presence of faulted Pliocene rocks [52].

2.1. Host Rock Petrology and Diagenesis

The petrology and diagenesis of sandstones and conglomerates of Montjuïc have been studied in detail before [39–42]. A brief summary is given in this subsection.

Siliciclastic rocks range from lithic to arkosic arenites/rudites to greywackes. Detrital grains are well-rounded and are composed of quartz (35%), potassium feldspar (9%), rock fragments (20%, mainly quartzites and schists) and minor muscovite, zircon, tourmaline, and biotite. The shale matrix, composed of illite-mica, is frequently transformed into opal and microquartz with variable amounts of remaining clay minerals. Porosity is low (1–3%), primary as intergranular or secondary due to the

dissolution of altered feldspar and shale matrix. Detrital fragments indicate that the source area most probably was the Collserola Massif (Figure 1), where Paleozoic rocks crop out.

Lithification of the Montjuïc sandstones was mostly due to the authigenesis of silica minerals. Silicification of these sandstones only occurred on high ground, as demonstrated by numerous boreholes around the mountain where these units appear non-silicified. On high ground, specifically in the Morrot area, the presence of some lenticular remnants of non-silicified rocks allows the observation that silicification fronts preferentially used coarse-grained sediments and fractures. Consequently, two main diagenetic facies with characteristic associations of authigenic minerals are identified: (i) the non-silicified and (ii) silicified facies. Non-silicified facies are constituted by ochre-colored fine-grained sandstones. In these facies, cementation is scarce and generally forms minor feldspar overgrowths around detrital k-feldspar as well as layers or nodules of calcite spar cement mainly filling interparticle porosity. Additionally, they present moldic porosity filled with calcite cement. Silicified facies are characterized by red to purple-colored coarse-grained sandstones containing opal, microquartz and quartz overgrowths as well as other minor authigenic minerals such as Ti and Fe oxides and alunite. Sparitic calcite cement filling residual porosity of silicified sandstones has also been described. Alunite and opal often appear at the boundary between silicified and non-silicified facies.

According to the aforementioned authors [39–42], the geological setting and the lack of compaction suggest that cementation occurred at shallow conditions by oxidizing groundwaters.
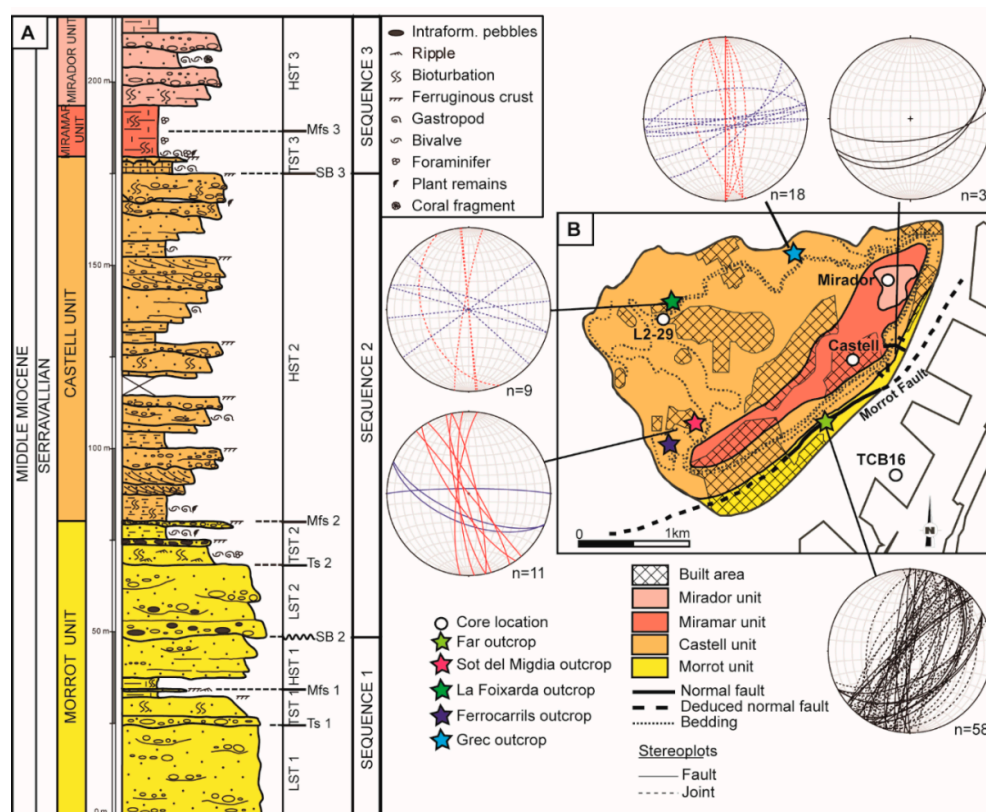
Figure 2. (**A**) General stratigraphic section of Montjuïc Hill [40]. (**B**) Arrangement of the lithostratigraphic units in the Montjuïc Hill [41] and Schmidt lower-hemisphere stereoplot projections of the different generations of fractures found in the study area. The three generations of fractures are indicated with different colors: set 1 (black), set 2 (blue), and set 3 (red).

3. Methodology

Five outcrops (Far, Sot del Migdia, La Foixarda, Ferrocarrils, and Grec) were chosen because of the good exposure of Miocene rocks affected by fracturing to study the fluid flow events related to

fracturing occurring in previously silicified rocks of the Montjuïc Hill. Moreover, access to four boreholes (L2-29, Castell, Mirador, and TCB16) allowed us to have a more representative lateral and vertical distribution of fracture-filling cements. Fractures were measured in the field and crosscutting relationships were established. Structural data were plotted and analyzed in lower hemisphere Schmidt stereoplots (Figure 2B). The different fracture-filling minerals developed in the different fracture systems were sampled in outcrops and boreholes for petrographic observations and geochemical analyses.

Thirty samples were collected from the outcrops and forty-eight samples were obtained from the four different boreholes. Thin sections were studied using optical and cathodoluminescence microscopes. A Technosyn Cold Cathodoluminescence Model 8200 MkII (Technosyn Limited, Cambridge, UK) operating at 16–19 kV and 350 µA gun current were used to establish the different calcite cement generations. Some thin sections were also examined under ESEM Quanta 200 FEI, XTE 325/D8395 scanning electronic microscope (FEI Europe B.V., Eindhoven, The Netherlands).

X-ray diffraction of bulk rock and oriented aggregates have been performed with a Bragg-Brentano PAnalytical X'Pert PRO MPD alpha 1(PANalytical B.V., Almelo, The Netherlands) operating at 1.5406 Å, 45 kV, and 40 mA in order to establish the mineralogy of fine-grained fracture fillings.

After the petrographic study, geochemical analysis of the different fracture-filling cements and host rock intergranular and moldic cements (elemental geochemistry, stable isotopes, and $^{87}Sr/^{86}Sr$ ratios) were carried out to characterize the different fluids (i.e., origin, pathways, fluid-rock interaction, temperature).

Carbon-coated thin sections were used for elemental analyses of carbonate and barite cements with a CAMECA model SX-50 microprobe (CAMECA SAS, Gennevilliers, France). It was operated using 15 nA of current intensity, 20 kV of acceleration voltage, and a beam diameter of 10 µm. The detection limits for carbonates are 99 ppm for Na, 554 ppm for Ca, 491 ppm for Mg, 223 ppm for Fe, 158 ppm for Mn, and 141 ppm for Sr. Detection limits (d.l.) for barites are 105 pp for Ca, 298 ppm for Co, 793 ppm for Sr, 1516 ppm for Ba, and 805 ppm for Pb. The precision of major elements is about 0.64% (at 2σ level).

Microsamples for oxygen, carbon, sulfur, and strontium isotope analysis were powdered with a 4 mm-diameter micro drill.

Collected samples for carbon and oxygen stable isotopes in carbonates were reacted with 100% phosphoric acid at 70 °C for two minutes in an automated Kiel Carbonate Device attached to a Thermal Ionization Mass Spectrometer Thermo Electron MAT-252 (Thermo Fisher Scientific, Bremen, Germany). The International Standard NBS-18 and the internal standard RC-1, traceable to the International Standard NBS-19, were used for calibration [53,54]. The results are expressed in δ‰ VPDB standard (Vienna Pee Dee Belemnite). Standard deviation is ±0.02‰ for $\delta^{13}C$ and ±0.05‰ for $\delta^{18}O$.

Oxygen isotopes were analyzed in ten samples of chalcedony and quartz cement and speleothems. The CO_2 to be analyzed was obtained by laser fluorination, using a CO_2 laser of 25 W and ClF_3 as a reactant, following the method of [55]. The obtained CO_2 was analyzed in a Dual Inlet SIRA-II mass spectrometer (VG-Isotech, Cheshire, UK). The results are expressed in δ‰ VSMOW standard (Vienna Standard Mean Ocean Water). These analyses were performed at the stable isotopic service of the Universidad de Salamanca.

Sulphur and oxygen isotopes were analyzed in ten barite samples to establish the origin of the precipitating fluid. The CO and SO_2 gases produced from the barites were analyzed on a continuous-flow elemental analyzer Thermo Delta Plus XP mass spectrometer (Thermo, Bremen, Germany), with a TC/EA pyrolyser for oxygen and a Finnigan MAT CHNS 1108 analyzer (Finnigan, Bremen, Germany) for sulfur. Results were calibrated with NBS-127, SO-5, and SO-6 international standards [56] and the internal standard YCEM (+12.78‰ CDT). The analytical error is ±0.4‰ CDT (Canyon Diablo Troilite) for $\delta^{34}S$ and ±0.5‰ VSMOW for $\delta^{18}O$.

The $^{87}Sr/^{86}Sr$ ratios of three barite samples were obtained. The Sr contained in the powder was obtained by means of chromatography using a SrResinTM (Triskem International). After

evaporation, samples were loaded onto a Re filament with 1 μL of 1M phosphoric acid and 2 μL of Ta$_2$O$_5$. Isotopic ratio measurements were carried out in a TIMS-Phoenix mass spectrometer (Isotopx, Cheshire, UK) with a dynamic multicollector during 10 blocks of 16 sweeps each, with an ^{88}Sr beam intensity of 3V. Isotopic ratios were corrected from ^{87}Rb interferences and normalized using a value of ^{88}Sr/^{86}Sr = 0.1194 to correct the possible mass fractionation during loading and analysis of the sample. During sample analysis, the isotopic standard NBS-987 was measured seven times obtaining a media of 0.710247 and a standard deviation 2σ of 0.000008. These values have been used for the correction of the analyzed values in the samples. Analytical error in the ^{87}Sr/^{86}Sr ratio is 0.01%. The standard deviation is 0.000003. These analyses were performed at the CAI (Centro de Apoyo a la Investigación) of Geochronology and Isotopic Geochemistry from the Universidad Complutense de Madrid.

4. Results

4.1. Fracturing

The Montjuïc Hill is affected by intense fracturing produced during the Neogene post-rift period (Langhian to present). Fractures are well-developed within the silicified areas whereas they disappear into the non-silicified areas. Three fracture sets have been distinguished according to their orientations, kinematics, and crosscutting relationships (Figures 2B and 3).
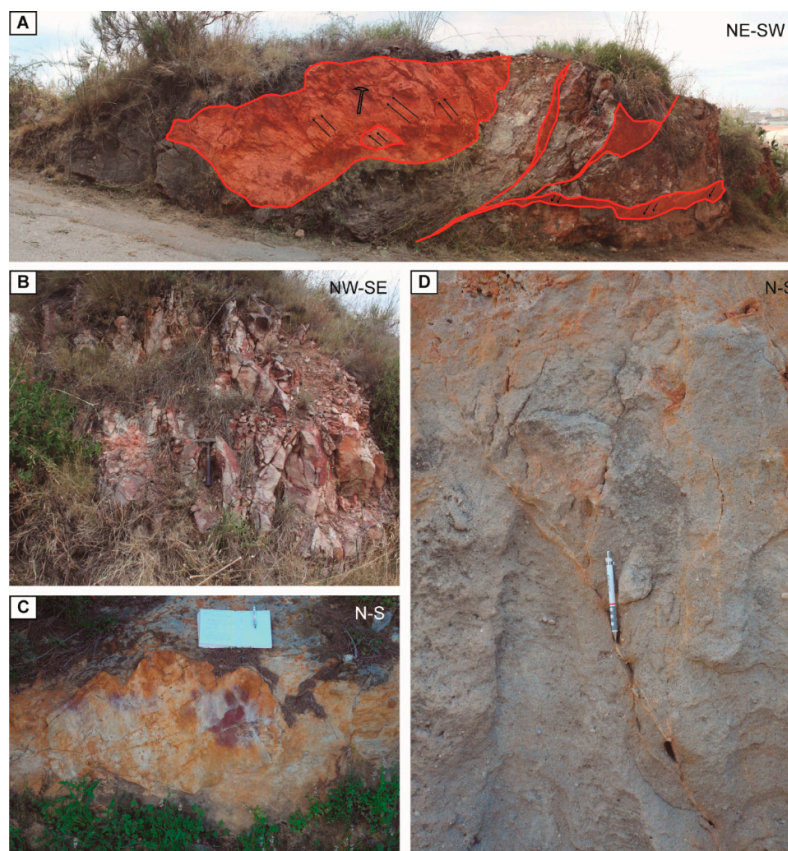
Figure 3. Outcrop photographs of the different fracture sets. (**A**) Interpreted outcrop view of the subsidiary fault zone of the Morrot fault in the far outcrop. Red areas highlight main fault planes and black arrows indicate the orientation and displacement direction of slickenlines. Rock hammer for scale. (**B**) Outcrop view perpendicular to the image shown in A. Sigmoidal shapes and alteration halos produced by iron oxides are observed. (**C**) Outcrop view of the second fracture set characterized by straight and discrete planes coated by orange and purple iron oxides. Ferrocarrils outcrop. (**D**)

Horsetail ending of a fault from the third fracture set partially filled with silica. Pen for scale. Ferrocarrils outcrop.

The first set of fractures is represented by NE–SW to NNE–SSW trending joints and normal and strike-slip faults with highly variable dips (Figure 2B). This array has been mainly observed in the southeastern part of the hill. In the far outcrop, a 20 m thick fault zone parallel and subsidiary to the Morrot fault is observed (Figure 3A,B). Individual planes are discrete and undulating, forming an arrangement of sigmoidal shapes that indicate dip-slip movement of the fault zone (Figure 3A,B). Fault planes show both dip-slip and strike-slip slickenlines, the latter being probably the result of the re-activation of the previous normal faults during the Messinian. Fault planes are cemented by silica and are surrounded by red to purple alteration halos towards the host rocks caused by the precipitation of iron oxides (Figure 3B). The second set of fractures is defined by E–W to WNW–ESE trending normal faults and joints dipping between 60 and 85° to both N and S (Figure 2B). They are characterized by straight to slightly undulating discrete planes (Figure 3C). Finally, the third set is constituted by N–S to NNW–SSE trending normal faults and joints with high dips (80–90°) to the E and W (Figure 2B). Commonly, these faults show horsetail endings (Figure 3D). Some fault planes of the second and third sets appear enlarged by dissolution and are cemented by silica minerals or filled with breccias cemented by silica, whereas other planes are coated by orange to purple iron oxides (Figure 3C,D).

4.2. Fracture Fillings

The fractures of the Montjuïc Hill contain different fillings depending on whether they are located in the non-silicified area, silicification front or in the silicified area.

Fractures in the non-silicified area are cemented by euhedral equant calcite crystals, ranging from 90 μm to 1 mm in size, that display a drusy texture (Figure 4A,B). Two calcite cement generations have been recognized. The first one, Cc1, shows a zoned bright orange to brown cathodoluminescence, similar to host rock intergranular cement, whereas the second generation, Cc2, has a uniform bright orange luminescence similar to that of cement filling molds (Figure 4B,C). The change between the two calcite cement generations in fractures is gradual.

Fractures within the silicification front are filled with clays with isolated grains of quartz and feldspar from the host rock (Figure 4D). This clayey filling has white or yellow to brownish color and it consists of sericite, kaolinite, goethite, and minor smectite and alunite.

In the silicified area, fractures display multi-episodic cementation produced by: (1) barite and (2) several silica varieties.

Barite cementation has been only identified in core L2-29 (Figure 2B) and in the Sot del Migdia outcrop (Figure 2B). Specifically, it is found along the uppermost 40 m below the present-day surface. It usually forms crusts up to 1 cm thick but in the L2-29 core, it completely fills a 30 cm-wide fracture. Barite cementation is characterized by the first stage of up to 300 μm-long prismatic crystals that grow decussated from the fracture wall and the second stage of up to 1 mm-long prismatic crystals that grow perpendicular to the fracture wall (Figure 5A). In some samples, in addition to barite, millimeter-sized cubic pyrite crystals and 20 to 50 μm long prismatic jarosite crystals are present. Pyrite crystallized either before the first barite generation or coevally during the last growth stage of this barite. Barite crystals of the second generation commonly have their margins replaced by chalcedony (Figure 5B). The presence of prismatic crystals with low relief next to quartz grains implies the complete replacement of barite by quartz.

With regard to silica cementation, the sequence opal → lussatite → chalcedony →quartz is recognized (Figure 5C), representing an increase in crystallinity and purity towards the inner part of fractures. Purity is defined by the presence of cations other than silica (mostly in low crystallinity silica varieties) but also by the presence of clay-sized particles of other minerals coming from the sandstone matrix. Three successive phases of opal precipitation have been identified according to the amount of lithic fragments, the content in titanium oxides, and the different degree of recrystallization to microquartz (Figure 5C,D). In some of the thickest veins, opal shows millimeter-

scale cracks and the silicic clasts develop both quartz rims and corrosion pits (Figure 5D,E). Lussatite has a fibrous texture, arranged in pseudospherulites, and usually forms single 20 to 35 μm-thick bands (Figure 5C,F). Chalcedony shows multiple precipitation episodes defined by 30 to 600 μm-thick bands constituted by fibers with radial disposition, spherulites or semispherulites (Figure 5F). It presents two varieties, chessboard chalcedony and chalcedonite. Finally, quartz precipitates in the remaining porosity as euhedral crystals (Figure 5F). Quartz crystals normally range between 20–70 μm in size but in some moldic porosity of the Castell cores (Figure 2B), they can reach 2 mm. This silica precipitation sequence locally alternates with precipitation of goethite (Figure 5G,H).

Breccias and internal sediment, cemented by the mineralogical sequence described above, are also present filling the fractures in the silicified area. Breccias are made of angular to subrounded clasts up to 3 cm in size. Sediments show a brownish color and were deposited as fine laminae at the base of fractures and on top of breccia clasts (Figure 6A,B). Geopetal structures are usually present (Figure 6C). These sediments comprise opal, smectite, iron oxides, barite, alunite and K-feldspar, and variable contents of host rock grains (0–60%).

In La Foixarda, Grec and Sot del Migdia outcrops, silica crusts, and stalactites are observed coating the fault planes (Figures 2B and 6D,G). Moreover, in the Grec outcrop flowstone speleothems are also present (Figure 6D). At least three generations of crusts are present and consist of 1 mm thick wavy layers of opal and chalcedony with different amounts of iron oxides inclusions (Figure 6E). Most stalactites are small (up to 7 mm long) and present several morphologies. Some of them are cylindrical, up to 2 mm in diameter, and formed by several concentric layers (Figure 6F). They do not show a drip-water channel through their length. Other stalactites display discontinuous and thin wavy "curtains" (Figure 6G), whilst some fracture planes are coated with mammillary microstalactites. The color of stalactites varies between grey, yellow and orange, probably due to the influence of small amounts of iron compounds.
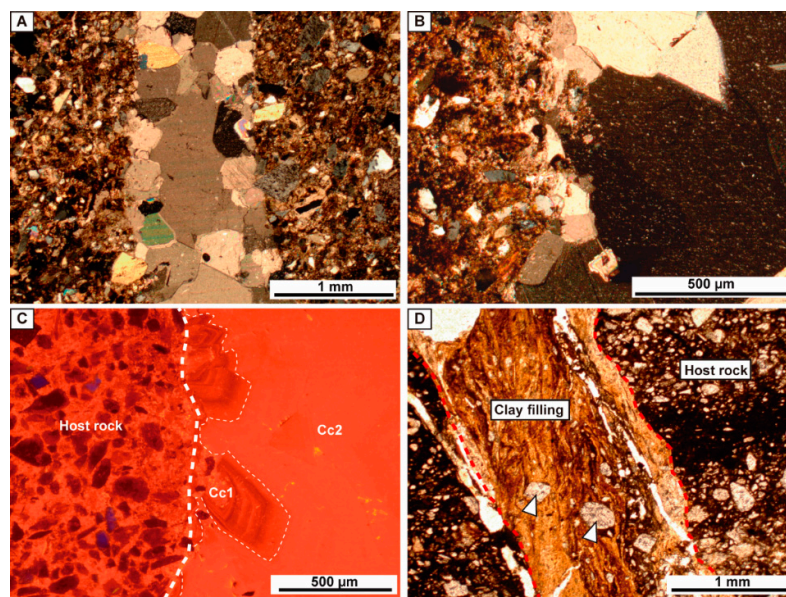

Figure 4. Fracture fillings from the non-silicified area and silicification front. (**A**) Fracture from the non-silicified area cemented by a drusy mosaic of equant calcite crystals (XPL). (**B,C**) Cross-polarized and cathodoluminescence images of a fracture from the non-silicified area filled with two generations of calcite cement. The fracture wall is marked with a white thick dashed-line. Note the gradual transition from the bright orange-brown zoned luminescence (Cc1) to the uniform bright orange luminescence (Cc2). The white thin dashed-line shows the limit between the two calcite generations. (**D**) Fracture from the silicification front, affecting reddish fine-grained sandstones due to the presence of iron oxide cement, filled with brownish clays and grains from the host rock (white arrows) (PPL). The limit between the host rock and the clayey filling has been marked with a red dashed-line.

Minerals 2020, 10, 135
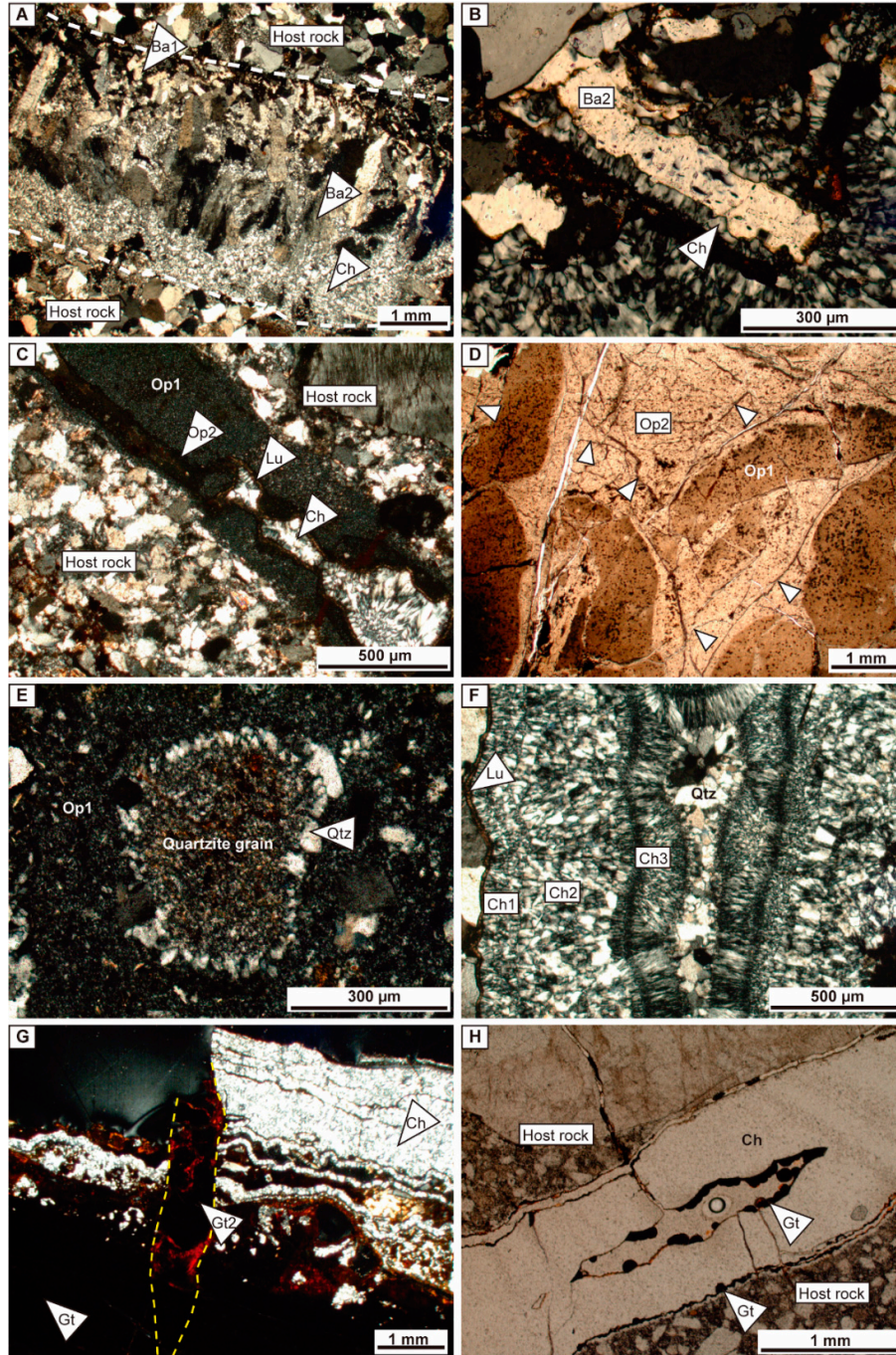
Figure 5. Cements in the fractures in the silicified area of the Castell Unit. (**A**) Fracture cemented by two generations of barite (Ba1 and Ba2) and a later generation of chalcedony (Ch) (XPL). Fracture walls are marked with a white dashed-line. (**B**) Detail of the replacement of barite (Ba2) by chalcedony (Ch) (XPL). (**C**) Silica varieties cementing a fracture according to their purity and crystallinity: two opal generations (Op1 and Op2), lussatite (Lu) and chalcedony (Ch) (XPL). (**D**) Fracture filled by two generations of opal affected by millimeter-scale cracks (white arrows). (**E**) Quartzite clast contained in a fracture cemented by opal that has developed a quartz rim (Qtz). (**F**) Fracture cemented by the silica sequence, lussatite, three generations of chalcedony and quartz (XPL). (**G**) Fracture filled by goethite (Gt) (and minor barite), alternation of goethite and chalcedony and finally pure chalcedony. The sequence is later cut by a fracture (yellow dashed- line) cemented by iron oxides (Gt2) (XPL). (**H**) Fracture cemented by several episodes of chalcedony and later goethite botryoids (PPL).
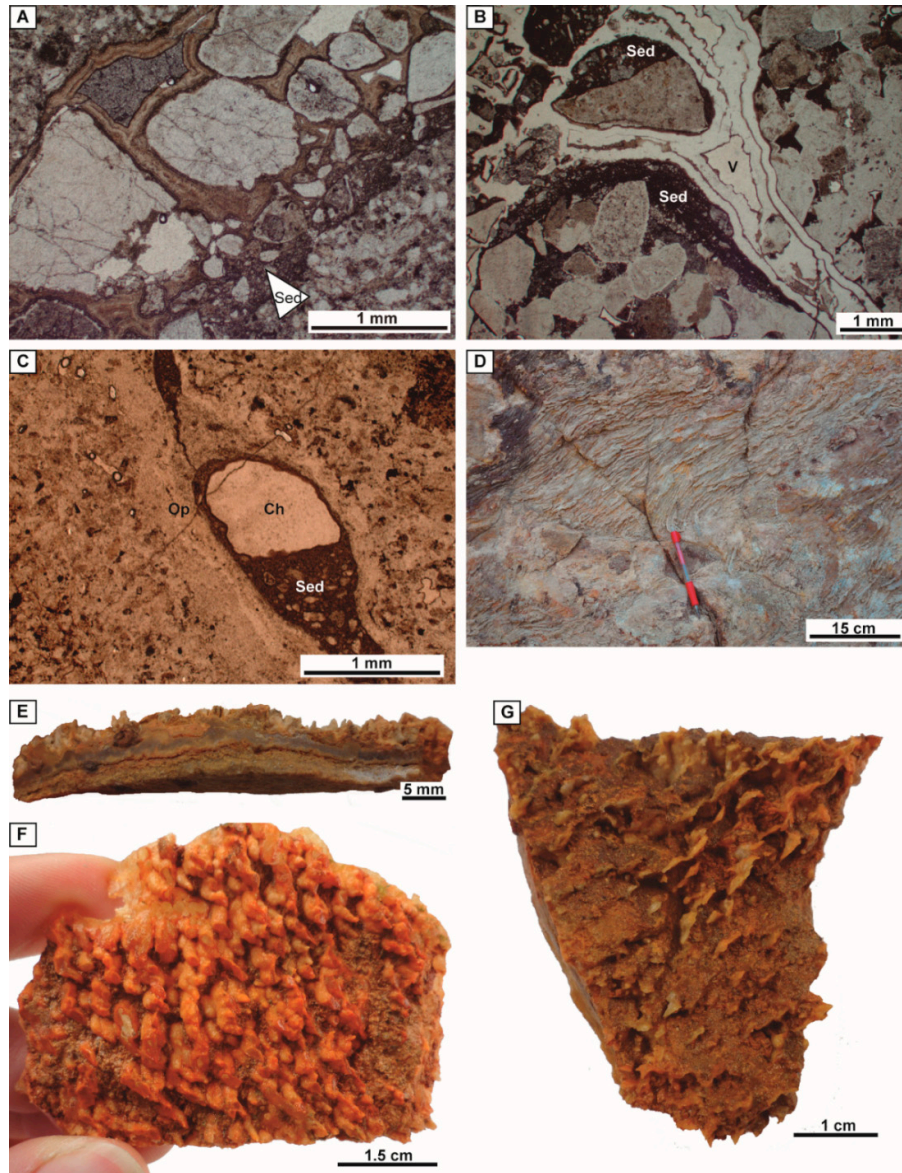
Figure 6. (**A**) Fracture filled with sediment (Sed) (deposited at the fracture bottom) and a microbreccia cemented by opal and lussatite (PPL). (**B**) Fracture filled with sediment and a microbreccia cemented by chalcedony. Some of the clasts contain earlier sediment fragments. V: void (PPL). (**C**) Geopetal structure filled with sediment at the base and chalcedony cement (Ch) at the top developed after opal cementation (Op) (PPL). (**D**) Cascade speleothems on a fault plane of the Grec outcrop. (**E**) Hand sample of several crust generations that pre-date stalactite formation. (**F**) Hand sample of cylindrical microstalactites. (**G**) Hand sample of small silica curtains.

4.3. Geochemistry

4.3.1. Elemental and Isotopic Composition of Barite

EPMA analyses revealed a large variation in barite composition, with Ba contents varying between 58.2% and 60.24%, Sr contents between 800 ppm and 1.36%, Ca contents between 100 and 700 ppm and Pb contents from below the detection limit to 700 ppm. Strontium and barium show a good negative correlation (R^2 = 0.832, n = 16), which reflects the isomorphous substitution of these elements in the barite-celestite solid solution (Figure 7A). Barites from the second generation that were replaced by silica show lower Sr contents than those that were not replaced.

Barite cement has δ^{34}S values ranging between +19.4‰ to +24.7‰ CDT in the core L2-29, whereas more δ^{34}S-enriched values, from +28.2‰ to +42‰ CDT, have been measured in the Sot del Migdia outcrop (Table 1). These values do not show covariation with δ^{18}O data, which ranges in both areas from +12.5‰ to +16.8‰ SMOW (Figure 7B). Barite has ^{87}Sr/^{86}Sr ratios varying between 0.712446 and 0.715218 (Table 1).

Table 1. Sulphur, oxygen, and strontium isotopes of barite cement.

Sample	δ^{34}S (‰CDT)	δ^{18}O (‰SMOW)	^{87}Sr/^{86}Sr	Location and Description
S29-12 A	23.8	13.4		L2-29 core at 35.20 m (±jarosite)
S29-12 B	22.6	12.5		L2-29 core at 35.20 m (+iron oxides)
S29-1	19.4	13	0.712446	L2-29 core at 37.85 m (+chalcedony)
S29-2	21.1	13.3		L2-29 core at 37.85 m (+chalcedony)
S29-14 B	22.7	15.4		L2-29 core at 39 m (+chalcedony)
S29-20 A	24.7	14.8		L2-29 core at 47 m. Next to fracture wall (+ch)
S29-20 B	13.1	13.2		L2-29 core at 47 m. Far from fracture wall (+ch)
MTJ-32 A	42	16.8	0.712939	Sot del Migdia. Next to fracture wall
MTJ-32 B	28.2	12.6		Sot del Migdia. Central part of the fracture
MTJ-32 C	34.2	13.8	0.715218	Sot del Migdia. Far from fracture wall
FMP-21a	30.7	12.9		Sot del Migdia
FMP-21b	41.9	15.2		Sot del Migdia
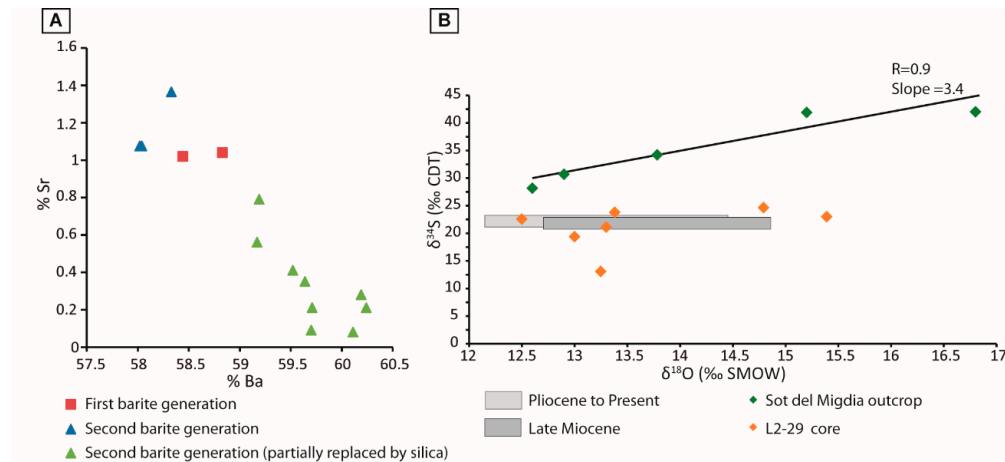

Figure 7. (**A**) Barite compositions plotted in a %Sr vs %Ba binary diagram. (**B**) δ^{34}S vs δ^{18}O binary diagram. Grey boxes represent the isotopic composition of seawater for the Late Miocene and from Pliocene to present according to [57].

4.3.2. Elemental and Isotopic Composition of Calcite Cements

Calcite cement Cc1, characterized by zoned cathodoluminescence, has Mg contents from below the detection limit to 2584 ppm, Mn and Fe from below the detection limit up to 7079 and 2028 ppm, respectively, and low Sr content (from below the detection limit to 665 ppm) (Table 2). The elemental composition of this calcite cement in fractures and intergranular porosity prior to silicification is very similar, although the latter reaches higher Fe contents (up to 24,189 ppm). Calcite cement Cc1 is characterized by δ^{18}O values between −10.5‰ and −6.7‰VPDB and δ^{13}C values between −5.8‰ and −1.7‰VPDB (Figure 8). Calcite Cc2, which cements fractures and molds, has higher Mn contents, from 1300 to 14,272 ppm, than cement Cc1. It has low Mg contents (average below the detection limit), Fe from below the detection limit to 3100 ppm, and very low Sr contents. Na is below the detection limit in both cement generations. Cement Cc2 has δ^{18}O values between −18.2‰ and −12.1‰VPDB and δ^{13}C values between −5.5‰ and −3.5‰VPDB (Figure 8).

Table 2. Elemental composition of calcite cements (<d.l.: below detection limit).

Cement Generation	Statistics	ppm Mg	ppm Ca	ppm Mn	ppm Fe	ppm Sr	ppm Na
	min	<d.l.	382,700	<d.l.	<d.l.	<d.l.	<d.l.
Cc1 Fractures	max	2584	403,564	7079	2028	665	<d.l.
n = 23	average	712	392,395	3452	645	285	<d.l.
	min	<d.l.	383,978	1300	<d.l.	<d.l.	<d.l.
Cc2 Fractures	max	2500	392,893	14,272	3100	400	<d.l.
n = 12	average	<d.l.	388,025	8288	669	228	<d.l.
Cc1 Intergranular	min	<d.l.	377,236	277	<d.l.	<d.l.	<d.l.
cement	max	1269	398,220	5885	24,189	1060	<d.l.
n = 17	average	611	390,352	3124	4263	351	<d.l.
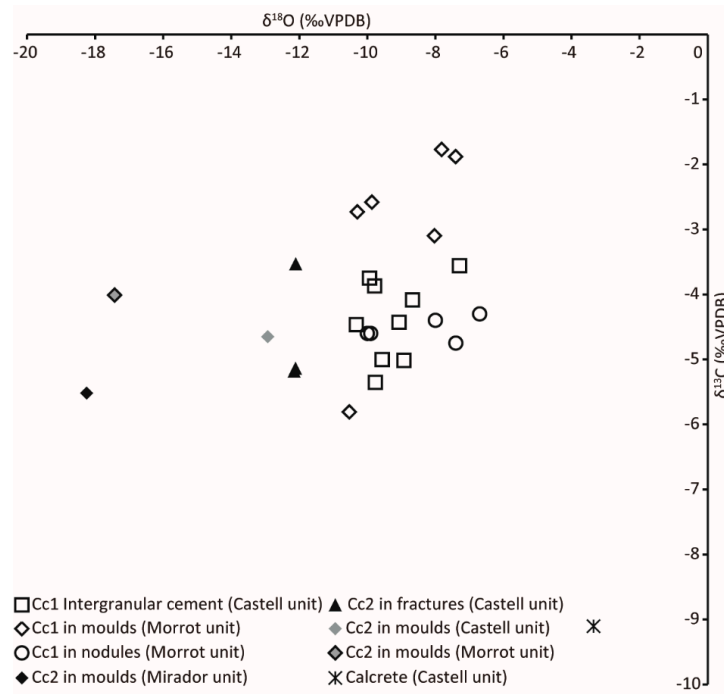
Figure 8. $\delta^{18}O$ vs $\delta^{13}C$ plot of calcite cements in fractures, molds and intergranular positions in the different stratigraphic units of the Montjuïc Hill.

4.3.3. Isotopic Composition of Silica Cements

Oxygen isotope measurements for chalcedony and quartz cements and speleothems yield similar values regardless of mineralogy. $\delta^{18}O$ values range from +9.2‰ to +25.2‰ SMOW (Table 3). The heaviest values are from speleothems of La Foixarda and El Far outcrops, which show a progressive enrichment in $\delta^{18}O$ (up to 11 units) towards the outer layers.

Table 3. Oxygen isotope values of silica cements and speleothems.

Sample	$\delta^{18}O$ (‰SMOW)	Location and Description
MTJ-31-1	16.4	Ferrocarrils. Chalcedony botryoids in fracture
MTJ-37-1	12.4	La Foixarda. Chalcedony stalactite nucleus
MTJ-37-2	23.4	La Foixarda. Chalcedony stalactite cover
MTJ-38-1	25.2	La Foixarda. Outer stalactitic layer
MTJ-38-2	22.3	La Foixarda. Inner stalactitic layer
MTJ-3A	18.8	El Far. Chessboard and fibrous chalcedony crosscut by iron oxides
S29-14A	9.2	L2-29 core. Chalcedony associated with barite in fracture
S29-17A	10.3	L2-29 core. Radial fibrous chalcedony
SR9B-03A	10	Castell core. Quartz in a vug

5. Discussion

The petrological study presented here has allowed us to establish the cementation sequence within the fractures of the Montjuïc Hill. In the silicified areas, the assemblage is barite followed by silica ± iron oxides, whereas in the non-silicified areas, cementation consists solely of calcite precipitation.

5.1. Origin of Calcite Cements

Calcite cements within the host rock and fractures record the diagenetic history previous to silicification.

Calcite cement Cc1 fills intergranular porosity, usually as nodules, moldic porosity, and fractures. The exclusive presence of this cement in the Morrot and Castell units probably indicates that its precipitation was prior to the sedimentation of the upper units and thus, formed relatively early. This is consistent with the formation of the calcite nodules, a feature most frequently associated with early diagenesis [2,58]. The oxygen isotope signature of this calcite cement, which ranges between –10.5‰ and –6.7‰ VPDB, is consistent with precipitation from meteoric water [59,60]. The zoned CL pattern may reflect variations in the oxidation state produced by oscillations of the water table level [61,62]. Several authors have proposed that carbonate shells are the main source of calcite cement in the concretions [63,64]. In this study, this observation is supported by the presence of shell molds and $\delta^{13}C$ values, which are consistent with a mixture of light carbon from soil-derived CO_2 [65] and heavier carbon derived from Miocene marine shells [66].

Calcite cement Cc2 has been identified in the Morrot, Castell, and Mirador units and yields more $\delta^{18}O$-depleted values, thus reflecting a variation in precipitation temperature or in water composition with respect to Cc1. If we consider that this oxygen depletion is due to burial, assuming a Miocene meteoric water composition of −7‰ SMOW [31] and applying the equation of [67], the precipitation temperature of this cement would be between 40 and 78 °C. With a regional geothermal gradient of 30 °C/km [68], these temperatures would imply a burial depth between 800 and 2100 m, which does not match the regional geology because late Miocene deposits do not exceed 500 m in thickness [43,69] and Plio-Pleistocene sediments were never deposited on top of the Montjuïc Hill [52]. The mechanical compaction of only the ductile clasts and the lack of chemical compaction [39–42] also support the hypothesis of the shallow burial of these rocks. Precipitation of calcite Cc2 from brine or from mixed meteoric and marine waters, both characterized by more $\delta^{18}O$-enriched values than meteoric water, would imply higher precipitation temperatures [67]. This leaves two options to explain the low $\delta^{18}O$ values at such shallow burial depths. Firstly, cement Cc2 precipitated from hydrothermal fluids, which have already been reported in several locations along the Catalan Coastal Ranges related to the Neogene extension [37,70,71], or secondly, the geothermal gradient may have been locally higher due to an increase of the lithospheric thinning towards the offshore, a fact that has been also suggested before [43,72,73].

5.2. Origin of Barite Formation in Fractures

Barite is only found in the fractures of the uppermost 40 m below the present-day surface, indicating their precipitation from at least one superficial fluid. Barites from the L2-29 core have $\delta^{18}O$ and $\delta^{34}S$ values consistent with the isotopic composition of seawater from the Late Miocene to present (from +12.2‰ to +14.9‰ SMOW and from +20.8‰ to +23.1‰ VCDT, according to [57]). However, barites from the Sot del Migdia outcrop show heavier $\delta^{34}S$ values than Late Miocene to present seawater. $\delta^{34}S$-enriched values indicate that the sulfate anion resulted from the microbial sulfate-reduction of seawater [74]. Such processes induced by microbial activity normally take place near the sediment-water interface but bioturbation, or fractures in our case, generate pathways for downward sulfate penetration [75–77]. In fact, the heaviest values have been obtained from outcrop rather than borehole samples (Table 1). Sulfate-reduction modifies both the sulfur and the oxygen signature, which could account for the oxygen values lying outside the range for seawater [78,79]. According to [79], the $\delta^{34}S/\delta^{18}O$ ratio can vary at different sites between 3.5 and 1.4 due to kinetic isotope effects

during sulfate reduction. In Figure 7B, barite samples from Sot del Migdia outcrop show a strong covariant trend (*R* = 0.9) with a slope of 3.4. The presence of jarosite in close association with barite and pyrite may indicate local H_2S reoxidation, which would lower the pH in order to precipitate this mineral. However, seawater could not be the superficial fluid controlling barite precipitation close to the surface. After the marine-transitional deposition of the Montjuïc sediments during the Langhian, host rock diagenesis occurred under meteoric conditions [42]. The ensuing marine transgression, recorded in the marine sediments within the Barcelona Plain, occurred during the Pliocene and did not affect these rocks as the uplift of the mountain commenced at this time [52]. Thus, as barite precipitation is limited to the fractures, seawater seemingly had to flow up through the faults. As observed by [80], seawater is not enough to precipitate barite and an external Ba-rich, sulfate-depleted fluid is also required. This fluid had to control the precipitation of barite close to the surface. Taking into account the uplift of the block and the proposed silicification model of the host rocks by means of meteoric groundwaters moving from the horst to the basin [39–42], such meteoric water is the most probable external fluid. The high $^{87}Sr/^{86}Sr$ ratios of barite (0.712446–0.715218), which are more radiogenic than those obtained from bivalves of the Morrot unit (0.708965) and seawater (0.709000, according to [66]), supports the meteoric character of these fluids [81]. K-feldspars and K-micas are the most common source of barium in sedimentary basins [80] and also of radiogenic strontium [82], and are important components within the basement granodiorites and phyllites and the Miocene siliciclastics filling the basin.

5.3. Origin and Age of Silicification in Fractures

The change from sulfate to silica precipitation indicates a change in water chemistry as the concentration of silica is low in sulfate-supersaturated waters [83,84]. Thus, considering the model of host rock silicification and barite precipitation, either the entrance of silica-rich meteoric groundwaters had to increase or the upflow through fractures of sulfate-rich waters had to stop in order to decrease silica solubility and start the process of fracture silicification [85].

The presence of stalactites demonstrates that these silica-rich fluids percolated downwards through the vadose regime. In addition, illuviation structures, as capping structures on top of breccia clasts formed by laminated and sorted sediment, and geopetal structures are indicative of water percolation near the surface. The presence of several generations of stalactites, illuviation structures together with the silica sequence, from opal to quartz, and corrosion gulfs indicates successive episodes of precipitation, dissolution, and redeposition of silica [86–88]. The cracks in opal cements can be interpreted as shrinkage cracks formed during such episodes. Both shrinkage cracks and quartz rims between host rock grains and the opaline matrix reveal initial precipitation of opal as a hydrated silica gel [85,87,89]. All these features and processes are very similar to those described in pedogenic silcretes [85,89–92], thus suggesting a shallow and low-temperature precipitation environment. The oxygen isotopic values of the outer layers of stalactites, which range between +22.3‰ and +25.2 ‰VSMOW, are in agreement with precipitation from low-temperature meteoric waters. Nevertheless, more depleted values as those registered in the nucleus, the first layers of stalactites and minor fractures in boreholes, which all vary between +9.2‰ and +16.4‰VSMOW, are not consistent with such an origin. One possible explanation is that contamination by other mineral phases could have occurred in samples collected close to the host rock or in very thin fractures, resulting in a different final isotopic signature. These can be silicate grains from the host rock, internal sediment deposited at the base of fractures or barite crystals, which grow close to the fracture wall and are disseminated between quartz and chalcedony crystals. Another option is that prior to meteoric percolation, an episode of hydrothermal fluids ascending through faults took place. However, this origin is difficult to reconcile with geotropic indications of a vadose environment. A third option is that the more depleted $\delta^{18}O$ values were linked to the depletion of meteoric waters during glacial periods [93] with the concomitant increase of the relative elevation and distance of the Montjuïc Hill to the coast.

The alternation between silica and iron oxides (Figure 5G) may reflect small fluctuations from reducing to oxidizing conditions, which favored the precipitation of iron derived from the

weathering of iron-rich minerals [94]. Such physico-chemical fluctuations were probably related to oscillations of the water table level produced by episodic rainfall/evaporation or seasonality (wet and dry periods) [87,95]. These climatic variations have in turn been proposed to explain the dissolution-precipitation cycles [85,87]. Thus, the model of fracture silicification would be the same as that proposed for silcretes by [87]: during dry periods, silica dissolution occurs due to alkaline conditions, whereas from the onset of the wet season, the entry of the acid rainwater lows the pH producing silica precipitation. Moreover, the precipitation of alunite, in the fractures of the silicification front and in capping sediments of the silicified area, required acidic conditions. The coexistence of opal, alunite, and kaolinite in the sediments and in the silicification front points to a pH between 3.5 and 5.5 [96]. Such a low pH would have been caused by the oxidation of iron sulfides during the onset of the wet season, resulting in the formation of H_2SO_4 that reacted with kaolinite, smectite, and illite to form alunite [87,97]. Iron sulfide oxidation is inferred from the presence of pyrite pseudomorphs transformed to iron oxides within the host sandstones.

Silica speleothems in the Montjuïc area formed in the meteoric vadose environment from the Pliocene, when uplift of the hill commenced, to recent (Quaternary) times, whereas present-day speleothems in Montjuïc are composed of calcite. It was suggested by [25,26] that, in some cases, low-temperature silica cements formed during cold periods due to the decrease of silica solubility at low temperatures. Particularly, [98] report the case of Fontainebleau sandstone diagenesis where silica cements precipitated during glacial periods. Alternate precipitation of quartz and low-crystallinity silica varieties depending on the temperature gradients of meteoric waters was found by [95]. Although silicification driven by glacial climates has been primarily linked to groundwater silicifications [26,98], a decrease of silica solubility in vadose meteoric waters during cold periods may have contributed to silica precipitation in fractures within silicified sandstones in the Montjuïc Hill. This linkage with glacial periods would support the third option proposed for the interpretation of $\delta^{18}O$ signatures and can explain why silica speleothems do not form nowadays. In fact, colder periods have been identified in post-Tortonian calcite speleothems in the Barcelona Plain [99] and in Pleistocene calcite speleothems in Mallorca [100] and southern Spain [101].

5.4. Karst Evidence: Silica Dissolution

Silica dissolution occurs at the micro-scale, as vug porosity (Figure 9A), and at the macroscale, as irregular caverns, both within the silicified host rock. The caverns, up to 60 cm in size, are formed at the intersection between discontinuity surfaces such as bedding planes and fractures (Figure 9B), confirming that such discontinuities act as important pathways for fluids causing preferential dissolution [102,103]. Thus, most silica precipitating within fractures is provided by the surrounding sandstones and conglomerates. At the micro-scale, dissolution preferentially affects the sandstone matrix constituted by opal and clays, feldspar and mica grains, and syntaxial feldspar overgrowths (Figure 9A,C). At fracture walls, dissolution normally starts along crystal borders so that sand grains are finally removed and included in the fracture by flowing water (Figure 9C,D). This process of dissolution, erosion, and winnowing of loose material by flowing waters has been described as "arenisation" [102,104–108]. In the Montjuïc Hill, arenisation is clearly triggered by dissolution, which is the dominant process, and therefore vugs and caverns are real karst forms and not pseudokarst features, which would imply a minor role of dissolution in their formation [102,109].
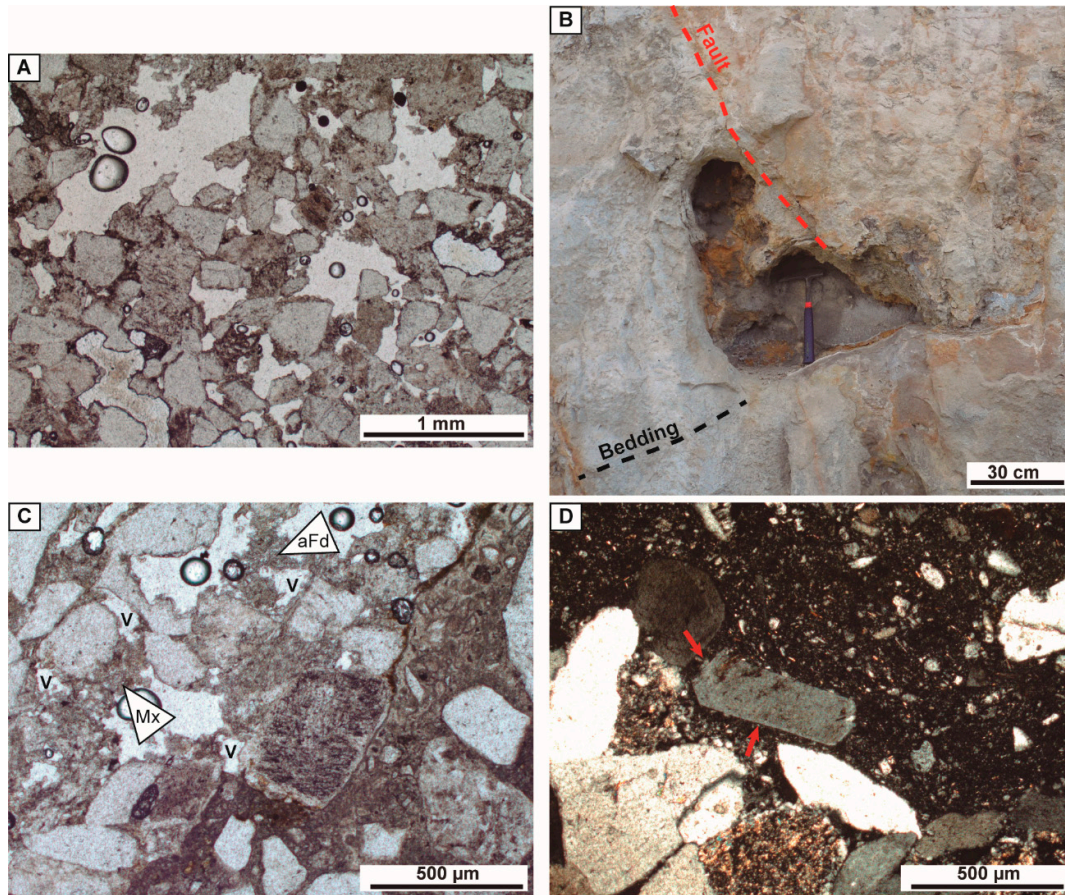
Figure 9. Evidence of in situ dissolution and arenisation. (**A**) Vuggy porosity. (**B**) Cavern porosity developed at the intersection between faulting and bedding. (**C**) Vuggy porosity (V) produced by the matrix (Mx) and altered feldspar (aFd) dissolutions in a sandstone sample. Note how the feldspar grain in the center of the image is about to be included in the fracture by dissolution around its borders. (**D**) Feldspar grain removed from the host rock and included in the fracture infilling by a process of dissolution around the grain boundaries (red arrows) and erosion (arenisation).

6. Conclusions

The fractures affecting the deltaic sequence of the Montjuïc Hill, formed after lithification and during the Montjuïc block uplift, show a complex diagenetic evolution controlled by the previous diagenesis of their host rocks.

Non-silicified areas are characterized by calcite cementation. Calcite cement Cc1 formed very early, prior to the sedimentation of the Miramar and Mirador units, and precipitated in molds, intergranular porosity (calcite nodules), and fractures from meteoric waters. Calcite cement Cc2, found in fractures and some molds, shows more $\delta^{18}O$-depleted values, which are interpreted as a result of a temperature increase linked to a higher geothermal gradient during the Neogene extension, rather than to overburden.

Fractures within the silicification front are filled by clays (sericite, kaolinite, goethite and minor smectite, and alunite) with isolated grains of quartz and feldspar from the host rock.

In silicified areas, fractures show multiepisodic cementation produced by barite and silica. Barite is only found in fractures along the uppermost 40 m below the present-day surface and precipitated from the mixing of upflowing marine fluids, as suggested by $\delta^{18}O$ and $\delta^{34}S$ values, and percolating meteoric waters, which supplied barium and more radiogenic $^{87}Sr/^{86}Sr$ ratios. $\delta^{34}S$ values heavier than those of Late Miocene seawater in a covariant trend with $\delta^{18}O$ indicate that microbial sulfate reduction occurred in outcrop samples. Silica cements follow the sequence opal, lussatite, chalcedony, and

quartz, all precipitated in the vadose zone from low-temperature percolating meteoric fluids as indicated by the presence of silica stalactites, illuviation, and geopetal structures and $\delta^{18}O$ values between +22.3‰ and +25.2 ‰VSMOW. Silica precipitation occurred in acidic conditions and under fluctuating redox conditions. A model of fracture silicification, similar to that of silcretes, and based on the alternation of dry and wet periods is proposed here. However, a decrease of silica solubility due to cold periods may also have contributed to silica precipitation, as indicated by $\delta^{18}O$ values between +9.2‰ and +16.4 ‰VSMOW and the present-day development of calcite speleothems and calcretes.

Dissolution occurs as vug porosity and caverns, which are generated by an arenisation process. Thus, silica precipitating within fractures was from the surrounding sandstones and conglomerates.

References

1. Karim, A.; Pe-Piper, G.; Piper, D.J.W. Controls on diagenesis of Lower Cretaceous reservoir sandstones in the western Sable Subbasin, offshore Nova Scotia. *Sediment. Geol.* **2010**, *224*, 65–83.

2. Morad, S.; Ketzer, J.M.; DeRos, F. Spatial and temporal distribution of diagenetic alterations in siliciclastic rocks: implication for mass transfer in sedimentary basins. *Sedimentology* **2000**, *47*, 95–120.

3. Ketzer, J.M.; Holz, M.; Morad, S.; Al-Aasm, I.S. Sequence stratigraphic distribution of diagenetic alterations in coal-bearing, paralic sandstones: Evidence from the Rio Bonito Formation (early Permian), southern Brazil. *Sedimentology* **2003**, *50*, 855–877.

4. El-ghali, M.A.K.; Mansurbeg, H.; Morad, S.; Al-Aasm, I.; Ajdanlisky, G. Distribution of diagenetic alterations in fluvial and paralic deposits within sequence stratigraphic framework: Evidence from the Petrohan Terrigenous Group and the Svidol Formation, Lower Triassic, NW Bulgaria. *Sediment. Geol.* **2006**, *190*, 299–321.

5. Worden, R.H.; Burley, S.D. *Sandstone Diagenesis: The Evolution of Sand to Stone*; Blackwell Publishing Ltd.: Hoboken, NJ, USA, 2009; ISBN 9781444304459.

6. Salem, A.M.; Ketzer, J.M.; Morad, S.; Rizk, R.R.; Al-Aasm, I.S. Diagenesis and Reservoir-Quality Evolution of Incised-Valley Sandstones: Evidence from the Abu Madi Gas Reservoirs (Upper Miocene), the Nile Delta Basin, Egypt. *J. Sediment. Res.* **2005**, *75*, 572–584.

7. Mansurbeg, H.; Morad, S.; Salem, A.; Marfil, R.; El-ghali, M.A.K.; Nystuen, J.P.; Caja, M.A.; Amorosi, A.; Garcia, D.; La Iglesia, A. Diagenesis and reservoir quality evolution of palaeocene deep-water, marine sandstones, the Shetland-Faroes Basin, British continental shelf. *Mar. Pet. Geol.* **2008**, *25*, 514–543.

8. Luo, J.L.; Morad, S.; Salem, A.; Ketzer, J.M.; Lei, X.L.; Guo, D.Y.; Hlal, O. Impact of diagenesis on reservoir-quality evolution in fluvial and lacustrine-deltaic sandstones: Evidence from jurassic and triassic sandstones from the Ordos Basin, China. *J. Pet. Geol.* **2009**, *32*, 79–102.

9. Morad, S.; Al-Ramadan, K.; Ketzer, J.M.; De Ros, L.F. The impact of diagenesis on the heterogeneity of sandstone reservoirs: A review of the role of depositional fades and sequence stratigraphy. *Am. Assoc. Pet. Geol. Bull.* **2010**, *94*, 1267–1309.

10. Khalifa, M.; Morad, S. Impact of structural setting on diagenesis of fluvial and tidal sandstones: The Bahi Formation, Upper Cretaceous, NW Sirt Basin, North Central Libya. *Mar. Pet. Geol.* **2012**, *38*, 211–231.

11. Sun, N.; Zhong, J.; Hao, B.; Ge, Y.; Swennen, R. Sedimentological and diagenetic control on the reservoir quality of deep-lacustrine sedimentary gravity flow sand reservoirs of the Upper Triassic Yanchang Formation in Southern Ordos Basin, China. *Mar. Pet. Geol.* **2020**, *112*, 104050.

12. Chan, M.A.; Parry, W.T.; Bowman, J.R. Diagenetic Hematite and Manganese Oxides and Fault-Related Fluid Flow in Jurass ic Sandstones, Southeastern Utah. *AAPG Bull.* **2000**, *84*, 1281–1310.

13. Ceriani, A.; Di Giulio, A.; Goldstein, R.H.; Rossi, C. Diagenesis associated with cooling during burial: An examplefrom Lower Cretaceous reservoir sandstones (Sirt basin, Libya). *Am. Assoc. Pet. Geol. Bull.* **2002**, *86*, 1573–1591.

14. Andre, G.; Hibsch, C.; Fourcade, S.; Cathelineau, M.; Buschaert, S. Chronology of fracture sealing under a meteoric fluid environment: Microtectonic and isotopic evidence of major Cainozoic events in the eastern Paris Basin (France). *Tectonophysics* **2010**, *490*, 214–228.

15. Cantarero, I.; Zafra, C.J.; Travé, A.; Martín-martín, J.D.; Baqués, V.; Playà, E. Fracturing and cementation of shallow buried Miocene proximal alluvial fan deposits. *Mar. Pet. Geol.* **2014**, *55*, 87–99.

16. Cruset, D.; Cantarero, I.; Travé, A.; Vergés, J.; John, C.M. Crestal graben fluid evolution during growth of the Puig-reig anticline (South Pyrenean fold and thrust belt). *J. Geodyn.* **2016**, *101*, 30–50.

17. Cruset, D.; Cantarero, I.; Vergés, J.; John, C.M.; Muñoz-López, D.; Travé, A. Changes in fluid regime in syn-orogenic sediments during the growth of the south Pyrenean fold and thrust belt. *Glob. Planet. Change* **2018**, *171*, 207–224.

18. Yuan, G.; Cao, Y.; Gluyas, J.; Cao, X.; Zhang, W. Petrography, fluid-inclusion, isotope, and trace-element constraints on the origin of quartz cementation and feldspar dissolution and the associated fluid evolution in arkosic sandstones. *Am. Assoc. Pet. Geol. Bull.* **2018**, *102*, 761–792.

19. Ulmer-Scholle, D.S.; Scholle, P.A.; Schieber, J.; Raine, R.J. *Memoir 109: A Color Guide to the Petrography of Sandstones, Siltstones, Shales and Associated Rocks*; Sweet, M.L., Ed.; The American Association of Petroleum Geologists: Tulsa, OK, USA, 2014; ISBN 978-0-89181-389-7.

20. Daza Brunet, R.; Bustillo Revuelta, M.Á. Exceptional silica speleothems in a volcanic cave: A unique example of silicification and sub-aquatic opaline stromatolite formation (Terceira, Azores). *Sedimentology* **2014**, *61*, 2113–2135.

21. Khalifa, M.A.; Mansurbeg, H.; Morad, D.; Morad, S.; Al-Aasm, I.S.; Spirov, P.; Ceriani, A.; De Ros, L.F. Quartz and Fe-dolomite cements record shifts in formation-water chemistry and hydrocarbon migration in Devonian shoreface sandstones, Ghadamis Basin, Libya. *J. Sediment. Res.* **2018**, *88*, 38–57.

22. Menezes, C.P.; Bezerra, F.H.R.; Balsamo, F.; Mozafari, M.; Vieira, M.M.; Srivastava, N.K.; de Castro, D.L. Hydrothermal silicification along faults affecting carbonate-sandstone units and its impact on reservoir quality, Potiguar Basin, Brazil. *Mar. Pet. Geol.* **2019**, *110*, 198–217.

23. Hervig, R.L.; Williams, L.B.; Kirkland, I.K.; Longstaffe, F.J. Oxygen isotope microanalyses of diagenetic quartz: possible low temperature occlusion of pores. *Geochim. Cosmochim. Acta* **1995**, *59*, 2537–2543.

24. Ullyott, J.S.; Nash, D.J. Micromorphology and geochemistry of groundwater silcretes in the eastern South Downs, UK. *Sedimentology* **2006**, *53*, 387–412.

25. Thiry, M.; Milnes, A.; Brahim, M. Ben Pleistocene cold climate groundwater silicification , Jbel Ghassoul region , Missour Basin , Morocco. *J. Geol. Soc. London.* **2015**, *172*, 125–137.

26. Thiry, M.; Milnes, A. Silcretes: Insights into the occurrences and formation of materials sourced for stone tool making. *J. Archaeol. Sci. Reports* **2017**, *15*, 500–513.

27. Tritlla, J.; Esteban, M.; Loma, R.; Mattos, A.; Sanders, C.; Vieira De Luca, P.H. Carrasco, A.; Gerona, M.; Herra, A.; Carballo, J. Where have most of the carbonates gone? Silicified Aptian pre-salt microbial (?) carbonates in South Atlantic basins (Brazil and Angola). In Proceedings of the Bathurst Meeting Mallorca 2019 16th International Meeting of Carbonate Sedimentologists, Palma de Mallorca, Spain, 9–11 July 2019.

28. Saller, A. Presalt lake evolution in the south Atlantic : the significance of microbial chert. In Proceedings of the Bathurst Meeting Mallorca 2019 16th International Meeting of Carbonate Sedimentologists Presalt, Palma de Mallorca, Spain, 9–11 July 2019.

29. Travé, A.; Calvet, F. Syn-rift geofluids in fractures related to the early-middle Miocene evolution of the Vallès-Penedès half-graben (NE Spain). *Tectonophysics* **2001**, *336*, 101–120.

30. Travé, A.; Calvet, F.; Soler, A.; Labaume, P. Fracturing and fluid migration during Palaeogene compression and Neogene extension in the Catalan Coastal Ranges, Spain. *Sedimentology* **1998**, *45*, 1063–1082.

31. Travé, A.; Roca, E.; Playà, E.; Parcerisa, D.; Gómez-Gras, D.; Martín-Martín, J.D. Migration of Mn-rich fluids through normal faults and fine-grained terrigenous sediments during early development of the Neogene Vallès-Penedès half-graben (NE Spain). *Geofluids* **2009**, *9*, 303–320.

32. Parcerisa, D.; Gómez-Gras, D.; Travé, a A model of early calcite cementation in alluvial fans: Evidence from the Burdigalian sandstones and limestones of the Vallès-Penedès half-graben (NE Spain). *Sediment. Geol.* **2005**, *178*, 197–217.

33. Parcerisa, D.; Gómez-Gras, D.; Martín-Martín, J.D. Calcretes, oncolites, and lacustrine limestones in Upper Oligocene alluvial fans of the Montgat area (Catalan Coastal Ranges, Spain). *Geol. Soc. Am. Spec. Pap.* **2006**, *416*, 105–117.

34. Baqués, V.; Travé, a.; Benedicto, a.; Labaume, P.; Cantarero, I. Relationships between carbonate fault rocks and fluid flow regime during propagation of the Neogene extensional faults of the Penedès basin (Catalan Coastal Ranges, NE Spain). *J. Geochemical Explor.* **2010**, *106*, 24–33.

35. Baqués, V.; Travé, A.; Roca, E.; Marín, M.; Cantarero, I. Geofluid behaviour in successive extensional and compressional events : a case study from the southwestern end of the Vallès-Penedès Fault (Catalan Coastal Ranges , NE Spain). *Pet. Geosci.* **2012**, *18*, 17–31.

36. Baqués, V.; Travé, a.; Cantarero, I. Development of successive karstic systems within the Baix Penedès Fault zone (onshore of the Valencia Trough, NW Mediterranean). *Geofluids* **2014**, *14*, 75–94.

37. Cantarero, I.; Travé, a.; Alías, G.; Baqués, V. Polyphasic hydrothermal and meteoric fluid regimes during the growth of a segmented fault involving crystalline and carbonate rocks (Barcelona Plain, NE Spain). *Geofluids* **2014**, *14*, 20–44.

38. Miró, J.; Martín-Martín, J.D.; Ibáñez, J.; Anadón, P.; Oms, O.; Tritlla, J.; Caja, M.A. Opaline chert nodules in maar lake sediments from Camp dels Ninots (La Selva Basin, NE Spain). In Proceedings of the Geo-Temas, Huelva, Spain, 12–14 September 2016; Volume 16, pp. 387–390.

39. Gomez-Gras, D.; Parcerisa, D.; Bitzer, K.; Calvet, F.; Roca, E.; Thiry, M. Hydrogeochemistry and diagenesis of Miocene sandstones at Montjuic, Barcelona (Spain). *J. Geochemical Explor.* **2000**, *69*, 177–182.

40. Gomez-Gras, D.; Parcerisa, D.; Calvet, F.; Porta, J.; Solé de Porta, N.; Civís, J. Stratigraphy and petrology of the Miocene Montjuïc delta: (Barcelona, Spain). *Acta Geològica Hispànica* **2001**, *36*, 115–136.

41. Parcerisa, D. Petrologia i diagènesi en sediments de l'Oligocè superior i del Miocè inferior i mitjà de la depressió del Vallès i del Pla de Barcelona, Universitat Autònoma de Barcelona: Barcelona, Spain, 2002.

42. Parcerisa, D.; Thiry, M.; Gomez-Gras, D.; Calvet, F. Tentative model for the silicification in Neogene Montjuic sandstones, Barcelona (Spain): authigenic minerals, geochemical environment and fluid flow. *Bull. La Soc. Geol. Fr.* **2001**, *172*, 751–764.

43. Roca, E.; Sans, M.; Cabrera, L.; Marzo, M. Oligocene to Middle Miocene evolution of the central Catalan margin (northwestern Mediterranean). *Tectonophysics* **1999**, *315*, 209–233.

44. Roca, E.; Guimerà, J. The Neogene structure of the eastern Iberian margin—Structural constraints on the crustal evolution of the Valencia trough (Western Mediterranean). *Tectonophysics* **1992**, *203*, 203–218.

45. Gaspar-Escribano, J.M.; Garcia-Castellanos, D.; Roca, E.; Cloetingh, S. Cenozoic vertical motions of the Catalan Coastal Ranges (NE Spain): The role of tectonics, isostasy, and surface transport. *Tectonics* **2004**, *23*, TC1004.

46. Calvet, F.; Travé, A.; Roca, E.; Soler, A.; Labaume, P. Fracturación y migración de fluidos durante la evolución tectónica neógena en el Sector Central de las Cadenas Costero Catalanas. *Geogaceta* **1996**, *20*, 1715–1718.

47. Julivert, M.; Duran, H. Paleozoic stratigraphy of the Central and Northern part of the Catalonian Coastal Ranges (NE Spain). *Acta Geol. Hisp.* **1990**, *25*, 3–12.

48. Llopis Lladó, N. Tectomorfología del macizo del Tibidabo y valle inferior del Llobregat. *Estud. Geográficos* **1942**, *3*, 321–383.

49. Roca, J.L.; Casas, A. *Gravimetria en zona urbana. Mapa Gravimétrico de la Ciudad de Barcelona; IV Asamblea Nacional de Geodesia y Geofísica. Presidencia de Gobierno. Comisión Nacional de Geodesia y Geofísica.* Comunicaciones: 28-9/2-10 Barcelona, Spain, 1981.

50. Blow, W.H. Late Middle Eocene to Recent planktonic foraminiferal biostratigraphy. In Proceedings of the First International Conference on Planktonic Microfossils, Geneva, Switzerland; Bronnimann, P., Renz, H.H., Eds.; Brill Archive: Leiden, The Netherlands, 1969; pp. 199–421.

51. BouDagher-Fadel, M.K. *Biostratigraphic and Geological Significance of Planktonic Foraminifera*; UCLPress: London, UK, 2018; ISBN: 978-1-910634-24-0.

52. Riba, O.; Colombo, F. *Barcelona: la Ciutat Vella i el Poblenou. Assaig de geologia urbana*; Institut d'Estudis Catalans i Reial Acadèmia de Ciències i Arts de Barcelona: Barcelona, Spain, 2009.

53. Friedman, I.; O'Neil, J.; Cebula, G. Two New Carbonate Stable-Isotope Standards. *Geostand. Newsl.* **1982**, *6*, 11–12.

54. Hut, G. *Consultants' Group Meeting on Stable Isotope Reference Samples for Geochemical and Hydrological Investigations*. International Atomic Energy Agency (IAEA): Vienna, Austria. 1987; p. 42.

55. Sharp, Z.D. A laser-based microanalytical method for the in situ determination of oxygen isotope ratios of silicates and oxides. *Geochim. Cosmochim. Acta* **1990**, *54*, 1353–1357.

56. Halas, S.; Szaran, J. Improved thermal decomposition of sulfates to SO_2 and mass spectrometric determination of $\delta^{34}S$ of IAEA SO-5, IAEA SO-6 and NBS-127 sulfate standards. *Rapid Commun. Mass Spectrom.* **2001**, *15*, 1618–1620.

57. Claypool, G.E.; Holser, W.T.; Kaplan, I.R.; Sakai, H.; Zak, I. The age curves of sulfur and oxygen isotopes in marine sulfate and their mutual interpretation. *Chem. Geol.* 1980, *28*, 199–260.

58. McBride, E.F.; Milliken, K.L.; Cavazza, W.; Cibin, U.; Fontana, D.; Picard, M.D.; Zuffa, G.G. Heterogeneous distribution of calcite cement at the outcrop scale in Tertiary sandstones, northern Apennines, Italy. *Am. Assoc. Pet. Geol. Bull.* **1995**, *79*, 1044–1063.

59. Moore, C.H. *Carbonate Diagenesis and Porosity. Developments in Sedimentology 46*; Elsevier Science Bv.: Amsterdam, The Netherlands,1989; ISBN 0444874151.

60. Tucker, M.E.; Wright, P.V. *Carbonate sedimentology*; Blackwell: Oxford, UK, 1990.

61. Rossi, C.; Canaveras, J.C. Pseudospherulitic fibrous calcite in paleo-groundwater, unconformity-related diagenetic carbonates (Paleocene of the Ager Basin and Miocene of the Madrid Basin, Spain). *J. Sediment. Res.* **1999**, *69*, 224–238.

62. Parcerisa, D.; Gómez-Gras, D.; Travé, A.; Martín-Martín, J.D. Fe and Mn in calcites cementing red beds: A record of oxidation–reduction conditionsExamples from the Catalan Coastal Ranges (NE Spain). *J. Geochemical Explor.* **2006**, *89*, 318–321.

63. Abdel-Wahab, A.; McBride, E.F.; Anonymous Origin of giant calcite-cemented concretions, Temple Member, Qasr El Sagha Formation (Eocene), Faiyum Depression, Egypt. *J. Sediment. Res.* **2001**, *71*, 70–81.

64. McBride, E.F.; Parea, G.C. Origin of highly elongate, calcite-cemented concretions in some Italian coastal beach and dune sands. *J. Sediment. Res.* **2001**, *71*, 82–87.

65. Cerling, T.E. The stable isotopic composition of modern soil carbonate and its relationship to climate. *Earth Planet. Sci. Lett.* **1984**, *71*, 229–240.

66. Veizer, J.; Ala, D.; Azmy, K.; Bruckschen, P.; Buhl, D.; Bruhn, F.; Carden, G. a. F.; Diener, A.; Ebneth, S.; Godderis, Y.; et al. 87Sr/Sr86, d13 C and d18 O evolution of Phanerozoic seawater. *Chem. Geol.* **1999**, *161*, 59–88.

67. Craig, H. The measurements of oxygen isotope paleotemperatures. In *Stable Isotopes in Oceanographic Studies and Paleotemperatures*; Consiglio Nazionale delle Richerche; Laboratorio di Geologia Nucleare; Tongiorgi, E., Ed.; Pisa: Rome, Italy, 1965; pp. 161–182.

68. Juez-Larré, J. Post late Paleozoic Tectonothermal Evolution of the Northeastern Margin of Iberia, Assessed by Fission-Track and (U-Th)/He Analyses. A Case History from the Catalan Coastal Ranges. Ph.D Thesis, Vrije Universiteit, Amsterdam, The Netherlands, 2003.

69. Alonso, F.; Peón, A.; Villanueva, O.; Rosell, J.; Trilla, J.; Obrador, A. *Mapa y Memoria Explicativa de la Hoja nº421 (Barcelona) del Mapa Geológico Nacional a Escala 1:50,000*; IGME: Madrid, Spain, 1977.

70. Carmona, J.M.; Bitzer, K.; López, E.; Bouazza, M. Isotopic composition and origin of geothermal waters at Caldetes (Maresme-Barcelona). *J. Geochemical Explor.* **2000**, *69–70*, 441–447.

71. Cardellach, E.; Canals, À.; Grandia, F. Recurrent hydrothermal activity induced by successive extensional episodes: The case of the Berta F-(Pb-Zn) vein system (NE Spain). *Ore Geol. Rev.* **2002**, *22*, 133–141.

72. Gallart, J.; Rojas, H.; Diaz, J.; Dañobeitia, J.J. Features of deep crustal structure and the onshore-offshore transition at the Iberian flank of the Valencia Trough (Western Mediterranean). *J. Geodyn.* **1990**, *12*, 233–252.

73. Vidal, N.; Gallart, J.; Dañobeitia, J.J. Contribution of the ESCI-Valéncia Trough Wide-Angle Data to a Crustal Transect in the NE Iberian Margin. *Rev. la Soc. Geol. Espana* **1997**, *8*, 417–429.

74. Seal, R.R. Sulfur Isotope Geochemistry of Sulfide Minerals. *Rev. Mineral. Geochemistry* **2006**, *61*, 633–677.

75. Fisher, I.S. Pyrite formation in bioturbated clays from the Jurassic of Britain. *Geochim. Cosmochim. Acta* **1986**, *50*, 517–523.

76. Chowdhury, A.H.; Noble, J.P.A. Organic carbon and pyrite sulphur relationships as evidences of bottom water conditions of sedimentation, Albert Formation fine-grained lacustrine sediments, New Brunswick, Canada. *Mar. Pet. Geol.* **1996**, *13*, 79–90.

77. Machel, H.G. Bacterial and thermochemical sulfate reduction in diagenetic settings—Old and new insights. *Sediment. Geol.* **2001**, *140*, 143–175.

78. Habicht, K.S.; Canfield, D.E. Sulphur isotope fractionation in modern microbial mats and the evolution of the sulphur cycle. *Nature* **1996**, *382*, 342–343.

79. Aharon, P.; Fu, B. Microbial sulfate reduction rates and sulfur and oxygen isotope fractionations at oil and gas seeps in deepwater Gulf of Mexico. *Geochim. Cosmochim. Acta* **2000**, *64*, 233–246.

80. Hanor, J.S. Barite-Celestine Geochemistry and Environments of Formation. *Rev. Mineral. Geochemistry* **2000**, *40*, 193–275.

81. Palmer, M.R.; Edmond, J.M. Controls over the strontium isotope composition of river water. *Geochim. Cosmochim. Acta* **1992**, *56*, 2099–2111.

82. Hanor, J.S. A model for the origin of large carbonate- and evaporite-hosted celestine (SrSO4) deposits. *J. Sediment. Res.* **2004**, *74*, 168–175.

83. Marshall, W.L.; Warakomski, J.M. Amorphous silica solubilities-II. Effect of aqueous salt solutions at 25°C. *Geochim. Cosmochim. Acta* **1980**, *44*, 915–924.

84. Marshall, W.L.; Chen, C.-T.A. Amorphous silica solubilities V. Predictions of solubility behavior in aqueous mixed electrolyte solutions to 300°C. *Geochim. Cosmochim. Acta* **1982**, *46*, 289–291.

85. Thiry, M.; Milnes, A.R.; Rayot, V.; Simon-Coinçon, R. Interpretation of palaeoweathering features and successive silicifications in the Tertiary regolith of inland Australia. *J. Geol. Soc. London.* **2006**, *163*, 723–736.

86. Thiry, M.; Milnes, A.R. Pedogenic and groundwater silcretes at Stuart Creek opal field, South Australia. *J. Sediment. Petrol.* **1991**, *61*, 111–127.

87. Blanco, J. a.; Armenteros, I.; Huerta, P. Silcrete and alunite genesis in alluvial palaeosols (late Cretaceous to early Palaeocene, Duero basin, Spain). *Sediment. Geol.* **2008**, *211*, 1–11.

88. Aubrecht, R.; Lánczos, T.; Gregor, M.; Schlögl, J.; Šmída, B.; Liščák, P.; Brewer-Carías, C.; Vlček, L. Sandstone caves on Venezuelan tepuis: Return to pseudokarst? *Geomorphology* **2011**, *132*, 351–365.

89. Thiry, M.; Millot, G. Mineralogical Forms of Silica and their Sequence of Formation in Silcretes. *SEPM J. Sediment. Res.* **1987**, *57*, 343–352.

90. Milnes, A.R.; Thiry, M. Silcretes. In *Weathering, Soils and Palaeosols. Developments in Earth Surface Processes 2*; Martini, I.P., Chesworth, W., Eds.; Elsevier: Amsterdam, The Netherlands, 1992; pp. 349–377.

91. Thiry, M.; Simon-Coinçon, R. Tertiary paleoweatherings and silcretes in the southern Paris Basin. *Catena* **1996**, *26*, 1–26.

92. Ullyott, J.S.; Nash, D.J.; Huggett, J.M. Cap structures as diagnostic indicators of silcrete origin. *Sediment. Geol.* **2015**, *325*, 119–131.

93. Bantcev, D. V.; Ganyushkin, D.A.; Chistyakov, K. V.; Volkov, I. V.; Ekaykin, A.A.; Veres, A.N.; Tokarev, I. V.; Shtykova, N.B.; Andreeva, T.A. The Components of the Glacial Runoff of the Tsambagarav Massif from Stable Water Isotope Data. *Geosciences* **2019**, *9*, 297.

94. Krumbein, W.C.; Garrels, R.M. Origin and Classification of Chemical Sediments in Terms of pH and Oxidation-Reduction Potentials. *J. Geol.* **1952**, *60*, 1–33.

95. Meyer, R.; Pena dos Reis, R.B. Paleosols and alunite in continental Cenozoic of western Portugal. *J. Sediment. Res.* **1985**, *55*, 76–85.

96. Raymahashay, B.C. A geochemical study of rock alteration by hot springs in the Paint Pot Hill area, Yellowstone Park. *Geochim. Cosmochim. Acta* **1968**, *32*, 499–522.

97. Wray, R. a L. Alunite formation within silica stalactites from the Sydney Region, South-Eastern Australia. *Int. J. Speleol.* **2011**, *40*, 109–116.

98. Thiry, M.; Schmitt, J.; Innocent, C.; Cojan, I. Sables et Grès de Fontainebleau: Que reste-t-il des faciès sédimentaires initiaux? In Proceedings of the 14ème Congrès Français de Sédimentologie, Paris, France, 4–8 November 2013; Association des Sédimentologues Français: Paris, France, Volume 74, pp. 37–90.

99. Cantarero, I.; Lanari, P.; Vidal, O.; Alías, G.; Travé, A.; Baqués, V. Long-term fluid circulation in extensional faults in the central Catalan Coastal Ranges: P–T constraints from neoformed chlorite and K-white mica. *Int. J. Earth Sci.* **2014**, *103*, 165–188.

100. Vesica, P.L.; Tuccimei, P.; Turi, B.; Fornós, J.J.; Ginés, a.; Ginés, J. Late Pleistocene Paleoclimates and sea-level change in the Mediterranean as inferred from stable isotope and U-series studies of overgrowths on speleothems, Mallorca, Spain. *Quat. Sci. Rev.* **2000**, *19*, 865–879.

101. Jiménez de Cisneros, C.; Caballero, E.; Vera, J. a.; Durán, J.J.; Juliá, R. A record of pleistocene climate from a stalactite, Nerja Cave, southern Spain. *Palaeogeogr. Palaeoclimatol. Palaeoecol.* **2003**, *189*, 1–10.

102. Wray, R.A.L. Quartzite dissolution: Karst or pseudokarst? *Cave Karst Sci.* **1997**, *24*, 81–86.

103. Sauro, F.; Lundberg, J.; De Waele, J.; Tisato, N.; Galli, E. Speleogenesis and speleothems of the Guacamaya cave, Auyan tepui, Venezuela. In Proceedings of the Karst and Caves in Other Rocks, Pseudokarst, 16th International Congress of Speleology: Brno, Czech Republic, 21–28 July 2013; pp. 298–304.

104. Martini, J.E.J. Karst in Black Reef Quartzite near Kaapsehoop, Eastern Transvaal. *Ann. South African Geol. Surv.* **1979**, *13*, 115–128.

105. Martini, J.E.J. Dissolution of quartz and silicate minerals. In *Speleogenesis: Evolution of Karst Aquifers*; Klimchouk, A.B., Ford, D.C., Palmer, A.N., Dreybrodt, W., Eds.; National Speleological Society: Huntsville, AL, USA, 2000; pp. 452–457.

106. Wray, R. A global review of solutional weathering forms on quartz sandstones. *Earth-Science Rev.* **1997**, *42*, 137–160.

107. Piccini, L.; Mecchia, M. Solution weathering rate and origin of karst landforms and caves in the quartzite of Auyan-tepui (Gran Sabana, Venezuela). *Geomorphology* **2009**, *106*, 15–25.

108. Sauro, F. Structural and lithological guidance on speleogenesis in quartz–sandstone: Evidence of the arenisation process. *Geomorphology* **2014**, *226*, 106–123.

109. Wray, R.A.L. Phreatic drainage conduits within quartz sandstone: Evidence from the Jurassic Precipice Sandstone, Carnarvon Range, Queensland, Australia. *Geomorphology* **2009**, *110*, 203–211.